Direct Numerical Simulation of Turbulent Heat Transfer Across a Mobile, Sheared Gas-Liquid Interface

D. Lakehal†

M. Fulgosi

G. Yadigaroglu

Institute of Energy Technology,
Swiss Federal Institute of Technology,
ETH-Zentrum/CLT, CH-8092 Zurich,
Switzerland

S. Banerjee

Department of Chemical Engineering,
University of California,
Santa Barbara, CA 93106, USA

The impact of interfacial dynamics on turbulent heat transfer at a deformable, sheared gas-liquid interface is studied using Direct Numerical Simulation (DNS). The flow system comprises a gas and a liquid phase flowing in opposite directions. The governing equations for the two fluids are alternately solved in separate domains and then coupled at the interface by imposing continuity of velocity and stress. The deformations of the interface fall in the range of capillary waves of waveslope $ak=0.01$ (wave amplitude a times wavenumber k), and very small phase speed-to-friction velocity ratio, c/u_*. The influence of low-to-moderate molecular Prandtl numbers (Pr) on the transport in the immediate vicinity of the interface is examined for the gas phase, and results are compared to existing wall-bounded flow data. The shear-based Reynolds number Re_* is 171 and Prandtl numbers of 1, 5, and 10 were studied. The effects induced by changes in Pr in both wall-bounded flow and over a gas-liquid interface were analyzed by comparing the relevant statistical flow properties, including the budgets for the temperature variance and the turbulent heat fluxes. Overall, Pr was found to affect the results in very much the same way as in most of the available wall flow data. The intensity of the averaged normal heat flux at high Prandtl numbers is found to be slightly greater near the interface than at the wall. Similar to what is observed in wall flows, for $Pr=1$ the turbulent viscosity and diffusivity are found to asymptote with z^{+3}, where z^+ is the distance to the interface, and with z^{+n}, where $n>3$ for $Pr=5$ and 10. This implies that the gas phase perceives deformable interfaces as impermeable walls for small amplitude waves with wavelengths much larger than the diffusive sublayers. Moreover, high-frequency fluctuating fields are shown to play a minor role in transferring heat across the interface, with a marked filtering effect of Pr. A new scaling law for the normalized heat transfer coefficient, K^+ has been derived with the help of the DNS data. This law, which could be used in the range of $Pr=1$ to 10 for similar flow conditions, suggests an approximate $Pr^{-3/5}$ relationship, lying between the $Pr^{-1/2}$ dependence for free surfaces and the $Pr^{-2/3}$ law for immobile interfaces and much higher Prandtl numbers. A close inspection of the transfer rates reveals a strong and consistent relationship between K^+, the frequency of sweeps impacting the interface, the interfacial velocity streaks, and the interfacial shear stress.
[DOI: 10.1115/1.1621891]

Keywords: Heat Transfer, Turbulence, Two-Phase, Interface

1 Introduction

Most investigations dealing with turbulent heat and mass transfer have traditionally focused on simple configurations involving rigid or flat surfaces. In practice, however, single-phase or two-phase flows may take place in the presence of boundaries which are neither flat nor rigid. In multi-phase flow systems involving immiscible fluids, the interface separating the fluids plays a role similar to that of an impermeable boundary. An example is the exchanges between the atmosphere and the oceans taking place across a continuously deforming interface. On a much smaller scale, gas-liquid exchange mechanisms across deformable interfaces may be encountered in annular flows, falling liquid films, etc.

Environmental studies on CO_2 absorption by the oceans [1,2] have focused on the proper scaling of the averaged mass transfer coefficient with the Reynolds and Prandtl/Schmidt numbers. The principle consists in relating local mass transfer rates and scalar fluxes to the properties of the fluctuating velocity field. The classical approach uses the analogy between diffusion of momentum and of a scalar quantity (heat or mass), extending Fick's gradient laws up to the turbulent regime, i.e., the scalar turbulent diffusivity, α_t, is made proportional to the turbulent viscosity, ν_t. The surface renewal theory [3] has also been widely employed to parametrize gas-liquid mass transfer rates. Its principle consists in relating the mass transfer rate to the time between sweeps and bursts (τ_{ren}) impinging on the interface, assumed to be responsible for surface renewal, i.e., $K \equiv (\mathcal{D}/\tau_{\text{ren}})^{1/2}$, where $\mathcal{D}=\nu/\text{Pr}$ refers to molecular diffusivity of heat (or mass by simply replacing Pr with Sc, the Schmidt number).

Heat and mass transfer at interfaces depends on the resistance of diffusive layers with thickness $\delta_L \sim O(0.01\,\text{mm})$ on the liquid side and $\delta_G \sim O(1\,\text{mm})$ on the gas side. Accordingly the transport across both layers is controlled by fine-scale turbulence, so that the transport mechanisms can be faithfully simulated only by the use of DNS. The complexity of the problems increases if the interface is further sheared and free to deform, in which case an

†To whom correspondence should be sent. E-mail: lakehal@iet.mavt.ethz.ch; Phone: +4116324613

Contributed by the Heat Transfer Division for publication in the JOURNAL OF HEAT TRANSFER. Manuscript received by the Heat Transfer Division July 17, 2002; revision received June 18, 2003. Associate Editor: K. S. Ball.

extra transverse motion superimposed on the mean flow is expected to occur in the direction normal to the interface. The continuously deformable interface could then affect the heat/mass transport indirectly by modifying the turbulence in the vicinity of the interface, or more precisely by increasing the portion of frictional drag transferred into form drag. The importance of such phenomenon is not yet clear, but a higher impact is expected if the surface is populated by capillary waves with wavelengths up to an order of magnitude larger than δ_G. For longer waves, the time scale over which the surface renews its structure becomes too large compared to the turbulence time scale, and the movement of the interface does not affect the transport phenomena. In summary, momentum and heat/mass transfer across deformable, sheared interfaces depends on the nature of the waves, and hence on the interfacial shear inducing them. An important question that arises then is whether the interfacial heat transfer scales with the friction velocity based on frictional drag and kinematic viscosity.

Although confined to simple configurations involving flat and non-deformable interfaces, early DNS studies proved particularly efficient in providing insight into the scalar exchanges all the way down to the diffusive sublayer. The contributions have generally concentrated on two aspects: a first group essentially focused on modeling turbulent convection mechanisms [4–7], while a second dealt with mass transfer [8,9]. Wall flow simulations at similar Reynolds numbers, but for different thermal boundary conditions, produced DNS data for the development and calibration of turbulent scalar convection models. The studies involving heat and mass transfer are the most relevant ones for the present contribution. Campbell and Hanratty [8], who pioneered this class of DNS, were interested in identifying the frequency fluctuations controlling most of the transfer at the wall. McCready et al. [9] re-investigated the problem considering a flat, mobile gas-liquid interface. Lyons et al. [6] simulated the case of differential heating between channel walls. Calmet and Magnaudet [10] showed that similar results can be obtained for Sc=200 by use of LES, supporting the fact that the effect of high-frequency turbulence near the wall is filtered out by increasing Pr or Sc [9]. Na et al. [7] studied the effect of the Prandtl number on turbulent statistics characterizing transport and the spatial variation of the variance of the fluctuating temperature. The very recent contribution of Piller et al. [11] examines the influence of low Prandtl numbers (0.025–1.0) on turbulent transport in channel flow. Their study has shown the molecular conductivity to act as a filter for high-frequency velocity fluctuations as Pr decreases, rendering them ineffective in the heat exchange processes.

Paralleling these studies, new results have been obtained in this area with the appearance of DNS of turbulent flows over wavy walls and sheared, gas-liquid interfaces [12–14]. Lombardi et al. [12] performed a DNS of coupled gas-liquid flows over a flat interface, which revealed that the interface appears to the gas phase almost like a rigid wall, whereas the liquid perceives the interface like a slip surface. De Angelis et al. [13] studied flows over rigid, sinusoidal wave trains. Their results show that fixed, high-amplitude waves exert significant effects on the mean flow and turbulence characteristics. De Angelis et al. [14] employed the same tools to study turbulent mass transfer at the sheared and deformable gas-liquid interface in the limit of capillary waves. A detailed comparison of the turbulence structure at the two different types of interface has been provided by Fulgosi et al. [15].

The objective of the present study is to complement the aforementioned contributions by exploring the heat transfer processes at a deformable interface, separating counter-flowing gas and liquid. The emphasis is on wave-induced mechanisms influencing the flow and the associated heat transfer in the context of low-to-moderate Pr numbers. The analysis is limited to the gas side, due to the presumed similarity between near-wall and near-interface turbulence. The effect of Prandtl number (Pr=1, 5 and 10) on the thermal field is investigated by means of a global analysis of the averaged heat fluxes, $\overline{u_i\theta}$, the temperature variance, $\overline{\theta^2}$, and the eddy diffusivity. Moreover, a scaling law for the heat transfer coefficient based on the effective viscous friction velocity is presented.

2 Mathematical Model and Numerical Strategy

The configuration of the problem is sketched in Fig. 1. The streamwise direction is denoted by *x*, the spanwise direction by *y* and the interface-normal (gravity) direction is referred to as *z*. The two phases are flowing counter-currently and are separated by an interface free to deform in three dimensions.

2.1 Transport Equations. The gas and liquid phases (designated by the subscripts *G* and *L*, respectively) are considered as Newtonian and incompressible fluids, flowing in separate domains, and driven by an imposed constant mean pressure gradient. The reference quantities employed for normalization in each domain are the effective shear velocity $u_*=\sqrt{\tau_{\rm int}/\rho}$, where $\tau_{\rm int}$ is the viscous interfacial shear stress, the half-depth of each computational domain *h*, and the kinematic viscosity ν. It is important to note that, at the beginning of the simulation when the interface is flat, the viscous interfacial shear stress balances exactly the mean pressure gradient driving the flow, and u_* corresponds to the shear velocity u_τ. As the waves start to form and develop, part of the energy is transferred into form drag, so that $u_*<u_\tau$.

The reference temperature T_* is defined as

$$T_*=\frac{q_{\rm int}}{\rho c_p u_*};\quad q_{\rm int}=-\lambda\left(\frac{d\overline{T}}{dz}\right)_{\rm int} \tag{1}$$

where $q_{\rm int}$ represents the interfacial heat flux. The time is made nondimensional using ν/u_*^2, and the length scales are normalized using u_*/ν. In each computational domain, the shear Reynolds number is defined as $\mathrm{Re}_*=u_*2h/\nu$.

With the reference quantities defined above, the Navier-Stokes and energy equations governing the flow in each domain can be written in nondimensional form as

$$\nabla\cdot\mathbf{u}^+=0 \tag{2}$$

$$\frac{\partial\mathbf{u}^+}{\partial t}+\nabla\cdot(\mathbf{u}^+\mathbf{u}^+)=-\nabla p^+ +\frac{1}{\mathrm{Re}_*}\nabla^2\mathbf{u}^+ \tag{3}$$

$$\frac{\partial T^+}{\partial t}+\nabla\cdot(\mathbf{u}^+T^+)=\frac{1}{\mathrm{Re}_*\,\mathrm{Pr}}\nabla^2T^+ +\frac{u^+}{2U_B^+} \tag{4}$$

where $\mathbf{u}^+=(u^+,v^+,w^+)$ is the nondimensional (by u_*) velocity vector, p^+ is the dynamic pressure normalized by ρu_*^2, T^+ is the nondimensional temperature defined as $T^+=(T-T_{\rm int})/T_*$, and U_B^+ is the mean bulk velocity. The last term in Eq. (4) is the source term needed to accurately predict the scalar transfer rate at low Prandtl numbers [4]. The conventional notation

$$\mathbf{u}^+(x,y,z,t)=\mathbf{U}^+(z)+u^+(x,y,z,t) \tag{5}$$

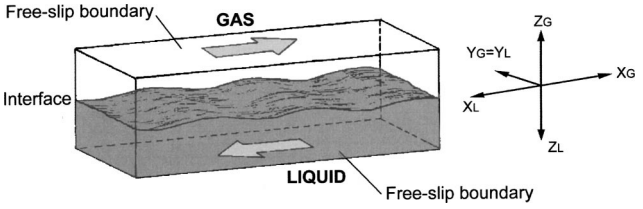

Fig. 1 Geometry of the simulated two-phase flow

$$T^+(x,y,z,t)=\Theta^+(z)+\theta^+(x,y,z,t) \tag{6}$$

is adopted to decompose the velocity and temperature fields into mean and fluctuating (turbulent) components.

2.2 Boundary Conditions. In the absence of phase change, the gas and liquid phases are coupled at the interface by the continuity conditions for normal and shear stresses, velocity and temperature (see, for example, Delhaye [16]), i.e.,

$$\begin{cases} \dfrac{1}{\mathrm{Re}_*}((\sigma_L^+-\sigma_G^+)\cdot\mathbf{n})\cdot\mathbf{n}+p_G^+-p_L^++\dfrac{1}{We}\nabla\cdot\mathbf{n}-\dfrac{1}{Fr}f^+=0 \\ ((\sigma_L^+-\sigma_G^+)\cdot\mathbf{n})\cdot\mathbf{t}_i=0, \quad i=1,2 \\ \mathbf{u}_L^+=\mathcal{R}\mathbf{u}_G^+ \\ T_G^+=T_L^+ \end{cases} \tag{7}$$

where σ^+ is the viscous stress tensor, f^+ is a measure of the vertical displacement of the interface with respect to the mid plane, $\mathbf{n}$ and $\mathbf{t}_i$ are the normal and the two tangential unit vectors, respectively, and $\mathcal{R}=\sqrt{\rho_L/\rho_G}$ is the density ratio parameter. The Weber (We) and Froude (Fr) numbers are defined as

$$\mathrm{We}=\frac{\rho_L h u_{*L}^2}{\gamma}, \quad \mathrm{Fr}=\frac{u_{*L}^2\rho_L}{gh(\rho_L-\rho_G)} \tag{8}$$

where γ is the surface tension.

The interface motion is simulated by solving a pure advection equation for the vertical elevation of the interface, $f(\mathbf{x},t)$, written in nondimensional form as

$$\frac{\partial f^+}{\partial t}+\mathbf{u}_L^+\cdot\nabla f^+=0 \tag{9}$$

The approach based on advecting Eq. (9) and solving for the gas and the liquid fields separately is a boundary fitting method. In contrast to interface tracking methods, this approach cannot be extended to strong topological changes of the interface that might lead to the inclusion of one phase into the other, such as fragmentation and wave breaking [17].

Periodic boundary conditions are applied in the streamwise (x) and spanwise (y) directions. At the outer boundaries, symmetry boundary conditions are employed for the thermal field, whereas free-slip boundary conditions are imposed on the velocity field.

2.3 Numerical Procedure. The governing equations are solved using a collocation pseudo-spectral technique employing Fourier series in the homogeneous, streamwise and spanwise directions, and Chebychev polynomials in the non-uniform direction normal to the interface. The physical domain is mapped into a rectangular parallelepiped at each time step. Equations (2), (3), and (4) are first solved separately in each domain, then coupled at the interface (identified by solving Eq. (9)) through the continuity conditions (7): on the gas side, the interfacial conditions apply to velocities and the temperature, whereas on the liquid side they apply to stresses and the temperature. Procedures for de-aliasing the solutions based on the two-thirds rule apply in this context, too.

A modified version of the two-step fractional time splitting method introduced by Temam [18] is employed. In the first step, an intermediate value for the velocity $\hat{\mathbf{u}}$ is determined by solving the momentum equation, without the pressure gradient term

$$\frac{\hat{\mathbf{u}}-\mathbf{u}^n}{\Delta t}+\sum_{q=0}^{J-1}\beta_q\nabla\cdot(\mathbf{u}\mathbf{u})^{n-q}-\frac{1}{2\,\mathrm{Re}_*}\nabla^2(\hat{\mathbf{u}}+\mathbf{u}^n)=0. \tag{10}$$

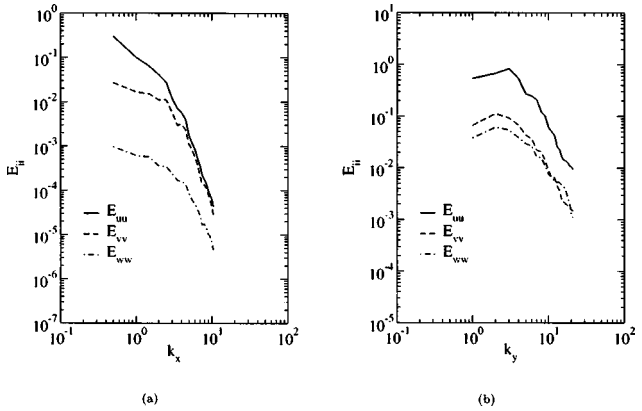

Fig. 2 Energy spectra at $z^+=5$ for the velocity components, in the gas phase: (*a*) streamwise direction; and (*b*) spanwise direction.

The convective term is explicit, with $J=2$, $\beta_0=3/2$ and $\beta_1=-1/2$, as in the Adams-Bashforth (AB) scheme. The viscous term is implicit and discretized using the Crank-Nicholson (CN) semi-implicit scheme. The time marching is second-order accurate in the computation of the intermediate velocity $\hat{\mathbf{u}}$, the value of which is corrected in the next step using

$$\frac{\mathbf{u}^{n+1}-\hat{\mathbf{u}}}{\Delta t}+\nabla p^{n+1}=0. \tag{11}$$

The unknown pressure field p^{n+1} can be obtained by taking the divergence of Eq. (11) which, using the condition that $\mathbf{u}^{n+1}$ is solenoidal, results in the Poisson equation

$$\nabla^2 p^{n+1}=\frac{1}{\Delta t}\nabla\cdot\hat{\mathbf{u}} \tag{12}$$

The energy Eq. (4) is also solved using a second-order accurate time differencing

$$\frac{T^{n+1}-T^n}{\Delta t}+\sum_{q=0}^{J-1}\delta_q\nabla\cdot(\mathbf{u}T)^{n-q}-\frac{1}{2\,\mathrm{Re}_*\,\mathrm{Pr}}\nabla^2(T^{n+1}+T^n)=0 \tag{13}$$

where the explicit ($J=2$, $\delta_0=3/2$ and $\delta_1=-1/2$) convective term is discretized using the AB scheme, and the implicit diffusive term is discretized by use of the CN scheme.

The size of each computational domain is $4\pi h\times 2\pi h\times 2h$ in streamwise, spanwise and interface-normal directions, corresponding to $1074\times537\times171$ wall units. As capillary waves do not produce significant domain distortion, a grid resolution (for each domain) of $64\times64\times65$ in the streamwise, spanwise and interface-normal directions was found to be appropriate for the solution of the isothermal flow field. This is proved in Fig. 2, displaying the energy spectra against wave numbers k_x and k_y for the three velocity components, evaluated at a distance of five wall units from the interface, in the gas side. The result shows no energy accumulation at high wave numbers, confirming that this resolution is sufficiently accurate for the solution of the velocity field. The extension of the spectrum to higher wave numbers, obtained by doubling the grid resolution in the interface-normal direction, did not show energy accumulation either (result not presented here). In their review of past DNS of heat transfer in channel flow, Piller et al. [11] note that the differences observed between some of the

Table 1 Computational parameters

	Pr=1	Pr=5	Pr=10
Re_*	171	171	171
We	4.8×10^{-3}	4.8×10^{-3}	4.8×10^{-3}
Fr	8.7×10^{-5}	8.7×10^{-5}	8.7×10^{-5}
$\Gamma=\sqrt{\rho L/\rho G}$	29.9	29.9	29.9
Grid points in each domain	64×64×65	64×64×129	64×64×129
Δx^+	16.77	16.77	16.77
Δy^+	8.38	8.38	8.38
Δz^+	0.102–4.191	0.026–2.096	0.026–2.096
Time Increment	$0.024\ \nu/u_*^2$	$0.012\ \nu/u_*^2$	$0.012\ \nu/u_*^2$

published results were chiefly due to insufficient statistical convergence, rather than to lower space resolution in the wall-normal direction.

2.4 Simulations. The shear Reynolds number Re_* is in each phase equal to 171. The inter-phase heat transfer does not include phase change. To limit the wave amplitude and steepness to the range of capillary waves, the Weber and Froude numbers were set equal to $We=4.8\times10^{-3}$ and $Fr=8.7\times10^{-5}$. The gas and liquid phases considered are such that $\mathcal{R}=29.9$. Three different thermal conditions have been investigated, namely Pr=1, 5 and 10. For Pr=1, the spatial resolution employed in each domain is 64×64×65 (hereinafter referred to as G1), whereas for Pr=5 and 10, it was doubled in the direction normal to the interface, i.e. 64×64×129 (referred to as G2). The grid resolutions in G1 ($\Delta x^+=16.77$, $\Delta y^+=8.38$, $\Delta z^+=0.102-4.191$) and G2 ($\Delta x^+=16.77$, $\Delta y^+=8.38$, $\Delta z^+=0.026-2.096$) are comparable to those employed by Tiselj et al. [19]. The time increments are $0.024\ \nu/u_*^2$ for the G1 grid, and $0.012\ \nu/u_*^2$ for G2.

After statistically stationary conditions were achieved in each run, the velocity and thermal fields were collected over $4000\nu/u_*^2$ nondimensional time units. The criterion used to establish steady state conditions was that the turbulent shear stress, $\overline{u^+w^+}$, and the turbulent heat flux, $\overline{w^+\theta^+}$, were no longer varying over a time interval of 1000 nondimensional time units. The simulation parameters are summarized in Table 1.

3 Interpretation of Results

Motivated by the uncertainties as to the existence of a similarity between near-wall and near-interfacial turbulence, Fulgosi et al. [15] studied the turbulent gas flow over the deformable interface, and compared the results to wall-bounded flow data at the same shear Reynolds number. In a time-averaged sense, the interfacial motion was seen to affect some features of the turbulence field in the near-interface region; the most pertinent effect is a general dampening of the turbulent fluctuating field which, in turn, leads to a reduction in the interfacial dissipation. Furthermore, the turbulence was found to be less anisotropic at the interface than at the wall. The analysis of the turbulent kinetic energy and Reynolds stress budgets revealed that the interface deformations mainly affect the so-called boundary term involving the redistribution of energy, and the dissipation terms, leaving the production terms almost unchanged. Away from the interface, the decomposition of the fluctuating velocity gradient tensor demonstrated that the fluctuating rate-of-strain and rate-of-rotation at the interface influence the flow throughout the boundary layer more vigorously.

Following this comparative strategy, in the present work, the interfacial turbulent heat transfer in the gas is investigated, and the results compared to wall-bounded flow data to reveal the effect of the interfacial deformation on heat transfer mechanisms for a range of low Prandtl numbers. As it is customary in DNS, the statistical analysis of the data is performed by averaging the collected velocity and thermal database over the two homogeneous directions (i.e., x-y plane average) and in time. For the flow under consideration here, this averaging procedure can be reliable only if the collected data cover a sufficiently large time interval over which the wave properties do not change. The statistical stationarity of the wave field is discussed below.

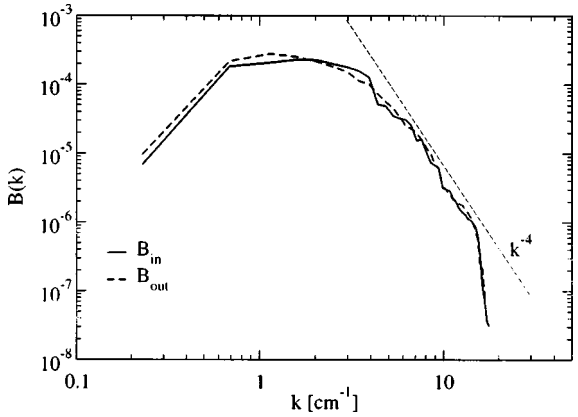

Fig. 3 Saturation spectra of the wave fields at the beginning (B_{in}) and at the end (B_{out}) of the sampling period

3.1 Characteristics of the Waves. The topology of the waves developing over a deformable free surface takes various forms, depending on the intensity of the interfacial shear stress caused by the nature of the underlying turbulence. The action of this shear is balanced by two stabilizing factors: one due to gravity and one caused by surface tension. The specialized literature [20] characterizes the wave field in terms of saturation spectrum

$$B(k)=k^2\Psi(k);\quad \Psi(k)=\frac{1}{2\pi}\int Z(\mathbf{r})e^{-i\mathbf{k}\cdot\mathbf{r}}dr, \qquad (14)$$

in which Ψ is the two-dimensional wave spectrum, and $Z(\mathbf{r})$ is the covariance of the instantaneous nondimensional surface displacement defined by

$$Z(\mathbf{r})=\overline{f(\mathbf{x},t_0)f(\mathbf{x}+\mathbf{r},t_0)} \qquad (15)$$

It is important to observe that, since the wavelength k is here defined in the dimensional space, Ψ has the dimension of $[L^2]$, so that a coefficient k^2 is needed in the definition of the saturation spectrum (14). The reader is referred to Phillips [20] for further theoretical details. The wave saturation spectra, obtained using grid G1, are plotted in Fig. 3 at two different times during the simulation: at the early stage (referred to as B_{in} in Fig. 3) and at the end (referred to as B_{out}) of the time interval over which the statistical analysis has been performed. The graph clearly indicates that the wave properties did not change significantly within this time interval, confirming the existence of the saturation or equilibrium range, which is synonymous to convergence in this context. The impact of the interfacial motion can then be inferred in an average sense.

3.2 Statistics of the Thermal Field. The mean temperature profiles plotted against the distance to the interface are shown in Fig. 4(*a*) for all Prandtl numbers. The results obtained by Kawamura et al. [5] at $Re_\tau=180$ for Pr=1 and Pr=5, and by Tiselj et al. [21] at $Re_\tau=171$ for Pr=1 and Pr=5.4 (for an isothermal wall boundary condition) have been included for comparison. For Pr=10 the present DNS has been compared to that of Na et al. [7] at $Re_\tau=150$. For Pr=1 the present results agree fairly well with both databases [5,21], whereas for Pr=5 the agreement is better with the data of Kawamura et al. [5] than with those of Tiselj et al. [21]. For Pr=10 the comparison with the data of Na et al.

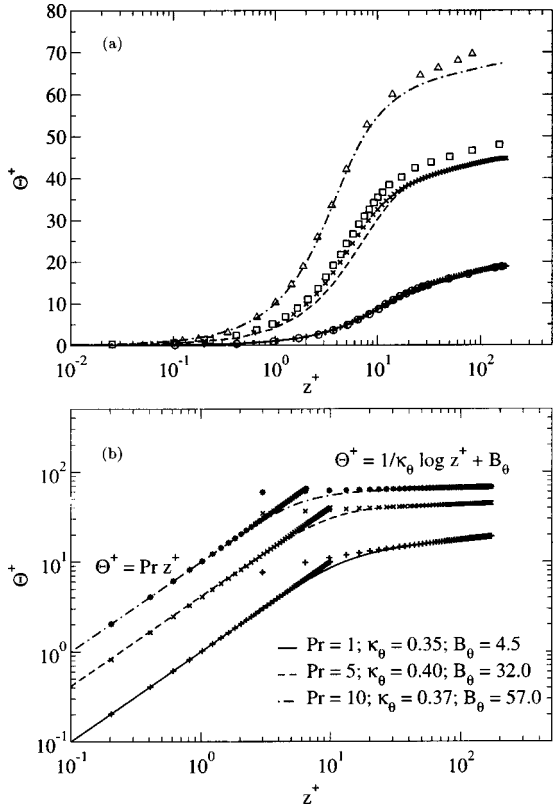

Fig. 4 Mean temperature profiles. (*a*) Comparison with other DNS databases. Lines are used to identify the present DNS result: ——, Pr=1; — — —, Pr=5; -·-·-, Pr=10. Symbols identify respectively: +, Pr=1 and ×, Pr=5: DNS of Kawamura et al. [5]; ○, Pr=1 and □, Pr=5: DNS of Tiselj et al. [21]; △, Pr=10: DNS of Na et al. [7]. (*b*) Present DNS extrapolated data; lines are used to identify present DNS results and symbols to identify the fitting equations.

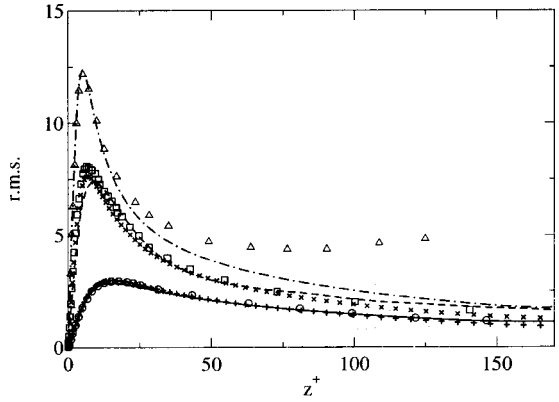

Fig. 5 Root mean square value of temperature fluctuations. Lines are used to identify the present DNS result: ——, Pr=1; — — —, Pr=5; -·-·-, Pr=10. Symbols identify respectively: +, Pr=1 and ×, Pr=5: DNS of Kawamura et al. [5]; ○, Pr=1 and □, Pr=5: DNS of Tiselj et al. [21]; △, Pr=10: DNS of Na et al. [7].

[7] is overall satisfactory. Figure 4(*b*) shows that inside the diffusive sublayer, the mean temperature profiles are in agreement with the linear relation $\Theta^+ = \mathrm{Pr}.Z^+$.

Further analysis of the data also permits to identify the extent of the logarithmic layer, where $\Theta^+ = 1/\kappa_\theta \ln z^+ + B_\theta$. Both the slope, κ_θ^{-1}, and the shift, B_θ, are found to vary with Prandtl number, though without leading to the establishment of a clear relationship. The diffusive sublayer exists in all three flows, with thicknesses Δ_θ^+ decreasing with increasing Prandtl number, i.e., $\Delta_\theta^+ \approx 6$, 4 and 2 wall units, respectively, for Pr=1, 5 and 10. While the results for Δ_θ^+ agree with those of Na et al. [7] and Kawamura et al. [5], those for the slope and the shift deviate appreciably from the data of Na et al. [7]. These deviations are perhaps due to the lower Reynolds number used by Na et al. [7] rather than the wall boundary conditions employed in their simulation. The difference in the slopes, in particular, suggests that the intensity of turbulence in [7] is simply weaker.

The behavior of the fluctuating temperature field near the wall/interface is generally accepted as a good indicator of the way scalar turbulent transport operates. An important feature requiring understanding is the effect of the Prandtl number on the interplay between molecular and turbulent transport near the wall. The r.m.s. values of the temperature fluctuations are presented in Fig. 5, where the results of Kawamura et al. [5] and Tiselj et al. [21] for Pr=1 and Pr=5, and those of Na et al. [7] for Pr=10, are again included for comparison. As can be observed, in both wall-bounded and interfacial flows, the increase in Prandtl number corresponds to a shift of the maximum of the temperature fluctuations towards the boundary. Both the present results and those of Kawamura et al. [5] for Pr=1, the maximum of the temperature fluctuations is located around $z^+ = 17$. Increasing the Prandtl number to 5 shifts the peak location to about $z^+ = 7$ in the wall-bounded flow, and to around $z^+ = 9$ in the flow over the deformable interface. The wall flow data of Na et al. [7] show the maximum of the temperature fluctuations located around $z^+ = 3$, whereas the present study shows that location to be around $z^+ = 5$. It is interesting to note that the exact location of the maximum r.m.s. value is not correlated with the position of the edge of the diffusive sublayer Δ_θ^+: the two locations tend to coincide with increasing Prandtl number.

The first important conclusion to be drawn from the above comparisons is that, as in wall flows, the most relevant statistical quantities scale with the friction velocity, based on frictional drag. The ratio of frictional drag to total drag (including form drag) was found to be around 0.98. The second important finding is the appreciable effect of Pr on $\overline{\theta^{+2}}$, indicating that the range of wave numbers in the thermal fluctuating field increases with Pr, for which the spectral functions of the velocity field are negligible.

3.3 Turbulent Fluxes and Inter-Phase Heat Exchange. Figure 6 shows the nondimensional averaged turbulent heat flux (THF), $\overline{u^+\theta^+}$, in the streamwise direction versus the dimensionless distance to the interface/wall. The data are compared to the wall-bounded flow DNS of Kawamura et al. [5]. For Pr=1 the streamwise THF over the deformable interface compares very

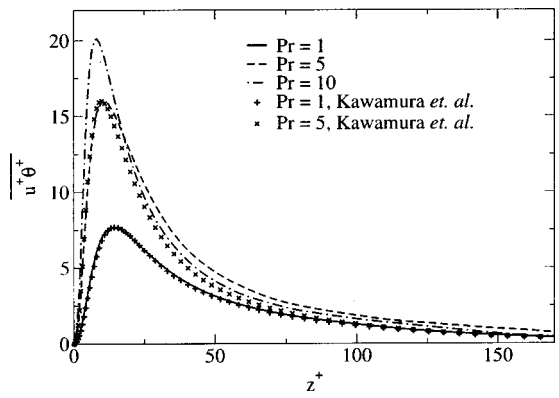

Fig. 6 Streamwise turbulent heat flux and comparison with Kawamura et al. [5]

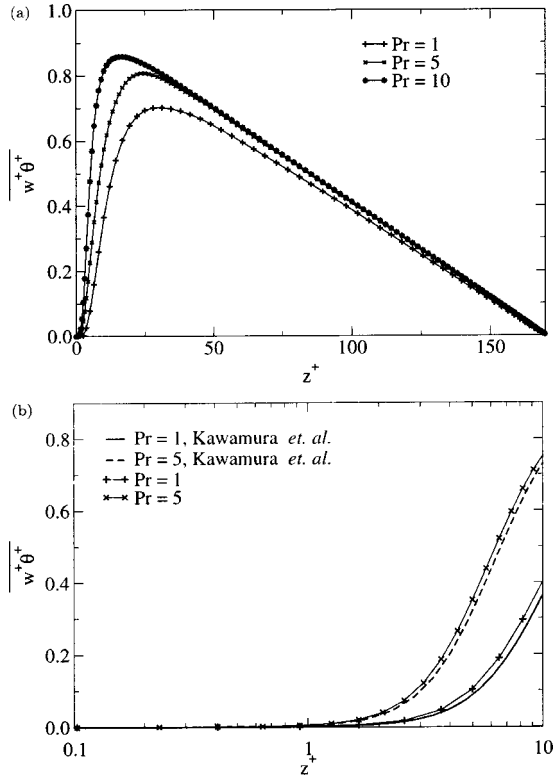

Fig. 7 Interface-normal turbulent heat flux: (*a*) boundary layer; and (*b*) near interface/wall region and comparison with Kawamura et al. [5].

well with the wall data; the behavior is similar and the peak value in both cases is located at the same distance from the interface/wall, $z^+ \approx 18$, which corresponds to the location of the maximum r.m.s. value of the temperature fluctuations. For Pr=5, the streamwise THF near the interface exhibits some differences compared to that near the wall, but peak values are almost identical and are furthermore reached almost at the same location from the interface/wall ($z^+ \approx 11$). Beyond the peak location, however, the THF for the flow over the deformable interface remains slightly higher than for the wall flow. For Pr=10 the streamwise THF peak location occurs at $z^+ \approx 8$. This analysis confirms that increasing the molecular Prandtl number substantially increases the intensity of the heat flux when approaching the wall/interface, depending on the thickness of the thermal boundary layer. Away from the diffusive thermal sublayer, the value of the THF drops faster for higher Prandtl numbers. Deeper in the bulk flow, heat transfer by turbulent transport does not depend much on the Prandtl number.

Figure 7(a) presents the distribution of the nondimensional averaged THF in the direction normal to the interface, $\overline{w^+\theta^+}$. We note that, as the molecular Prandtl number increases, the peak location moves closer to the interface, and so does the intensity of the flux. The differences between the near-interface and near-wall values (at $z^+ < 10$) of the normal THF are analyzed in detail in Fig. 7(*b*). For both Pr=1 and Pr=5 the flux intensity near the deformable interface is higher than at the wall. This implies that the interfacial dynamics leads to an increase in the vertical THF as compared to the situation near the rigid wall. The only plausible explanation for this difference is that the waves promote the velocity fluctuating field normal to the interface. Fulgosi et al. [15] indeed report that the turbulent kinetic energy decays faster at the

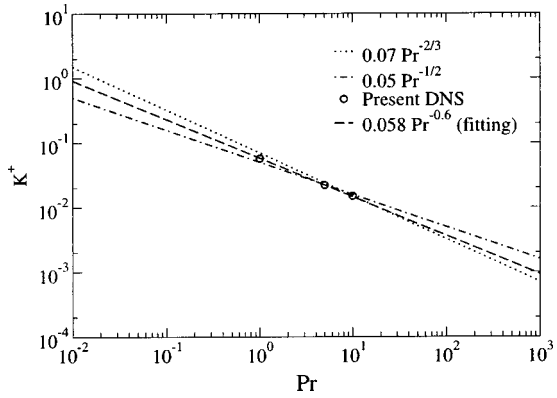

Fig. 8 Heat transfer coefficient

wall than at the mobile interface. The differences between the streamwise and vertical THFs will be explained more fully in Section 3.5, where the budget equations for the heat fluxes are compared term by term.

The nondimensional heat transfer coefficient (HTC) is defined as

$$K^+ = \frac{q_{int}}{\rho c_p \Delta \overline{T} u_*} = \frac{1}{Pr} \frac{1}{(T_{top} - T_{int})} \left. \frac{d\overline{T}}{dz^+} \right|_{int}, \qquad (16)$$

where $\overline{T}_{top}$ represents the mean temperature at the upper boundary of the gas domain (in [22], $\overline{T}_{top}$ was taken at the center of the closed channel). Note, too, that K^+ is normalized by the effective friction velocity associated with a frictional drag $u_* = 0.98 u_\tau$. The scaling of the heat transfer coefficient with the effective frictional velocity u_* has so far shown that it scales with $Pr^{-1/2}$ at mobile interfaces, and with $Pr^{-2/3}$ at immobile interfaces [9]. De Angelis et al. [14] have shown the $Pr^{-2/3}$ scaling to also hold on the gas side of wavy gas-liquid interfaces, but for high-Sc numbers only.

Figure 8 presents the values of the nondimensional HTC obtained for the gas side in the present DNS as a function of Prandtl number. For the range of Pr investigated here, the present DNS provides the following variation of the HTC

$$K^+ = 0.058 \ Pr^{-3/5}, \qquad (17)$$

which can be seen to vary between $\propto Pr^{-1/2}$ for free surfaces and $\propto Pr^{-2/3}$ for immobile interfaces for much higher Prandtl numbers. For instance, the DNS of Na et al. [7] delivered smaller values for both the coefficient of proportionality and the exponent, i.e., 0.0509 and 0.546, respectively. A parameterization of the scalar transfer rate by reference to the surface renewal theory, using the above result, yields

$$K^+ = 0.41 \ \tau_{ren}^{+\,-0.5} \ Pr^{-0.6}, \qquad (18)$$

where the normalized (by ν/u_*^2) mean time between sweeps, τ_{ren}^+, given by the DNS is approximately equal to $f_{sweep}^{-1} = 50$, where f_{sweep} denotes the frequency of sweeps ejections. Banerjee [23] obtained a similar relationship for high-Sc mass transfer at solid walls based on the Leveque boundary layer solution, reading

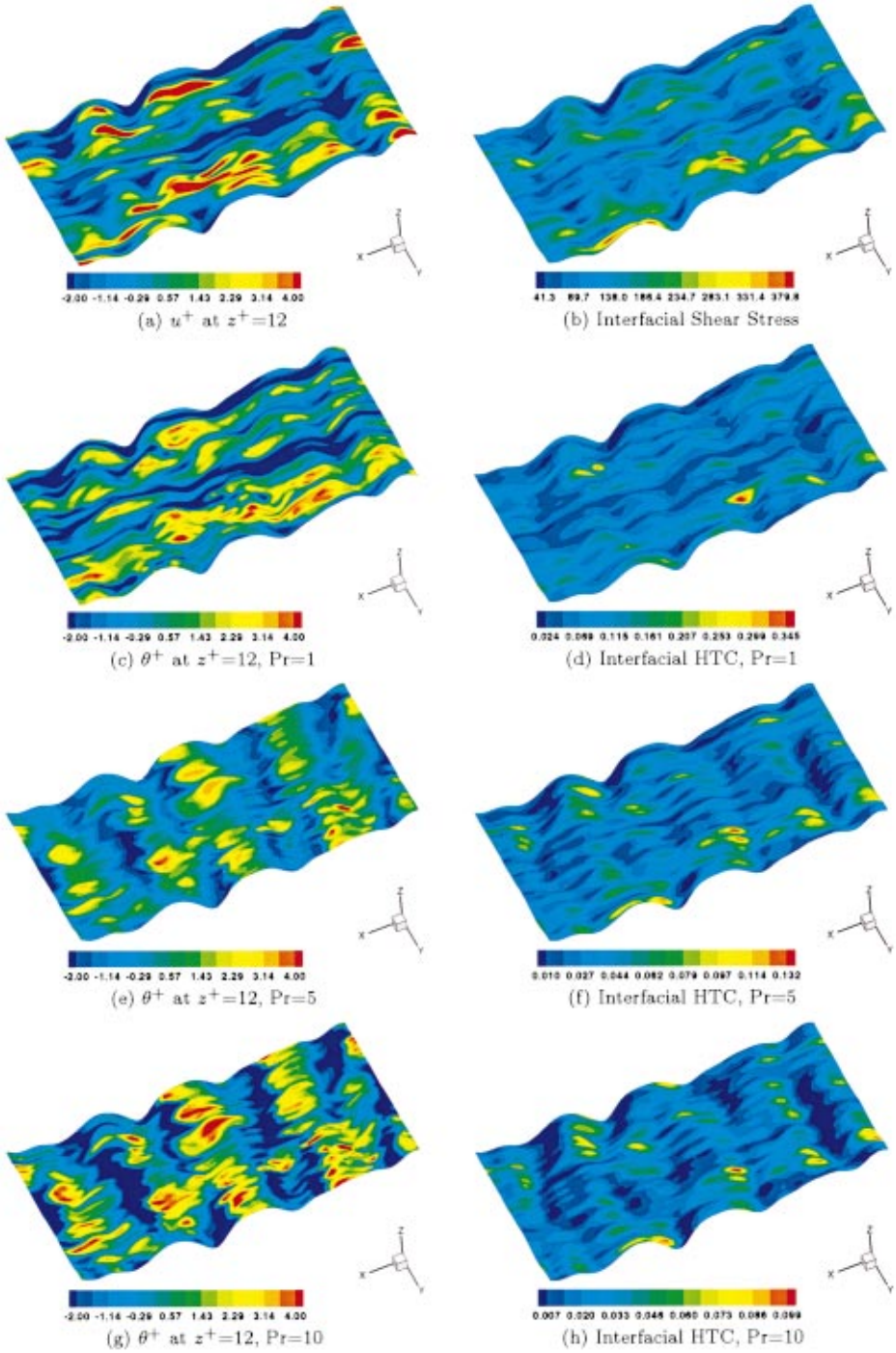

Fig. 9 The elevation of the waves is amplified by factor 10: (*a*) u^+ at $z^+=12$; (*b*) interfacial Shear Stress; (*c*) θ^+ at $z^+=12$, Pr=1; (*d*) interfacial HTC, Pr=1; (*e*) θ^+ at $z^+=12$, Pr=5; (*f*) interfacial HTC, Pr=5; (*g*) θ^+ at $z^+=12$, Pr=10; and (*h*) interfacial HTC, Pr=10.

$$K^+ = 0.68\ \tau_{\mathrm{ren}}^{+\,-0.5}\ \ \mathrm{Sc}^{-0.66}, \tag{19}$$

in which both the constant and the Sc power are actually functions of the Schmidt number. A close inspection of the Polhausens's boundary layer solution reveals on the other hand that the best fit for *Sc* in the range of Pr=5 to 15 is obtained with the constant fixed to 0.6 and the Sc exponent to -0.6.

Contours of the instantaneous HTC at the interface are shown in Figs. 9(*d*), 9(*f*), and 9(*h*), for Pr=1, 5 and 10, respectively, and are compared with the thermal streaks represented by contours of θ^+ at $z^+=12$, shown in the neighboring left panels (Figs. 9(*c*), 9(*e*), 9(*g*)). The comparison also includes contours of instantaneous velocity streaks, marked by contours of u^+ at $z^+=12$ (Fig. 9(*a*)), and of the instantaneous shear stress at the interface (Fig. 9(*b*)). The three-dimensional interfacial waves can be seen to develop and propagate in the direction of the gas-flow (in the pictures the wave amplitude has been magnified by a factor ten). Regions of high shear-high heat transfer rates at the crests can be clearly distinguished from regions of low shear-low heat transfer rates at the troughs. The streaky structure of the velocity field is

well represented by contours of u^+, similar to what is observed in wall flow [24], and is shown to conform to the thermal streaks for Pr=1. This result indeed confirms the Reynolds analogy between diffusion of momentum and diffusion of heat; the deviations become evident with increasing Prandtl number.

Observing the HTC contours also reveals that heat transfer rates correlate with the interfacial shear; the largest values, occurring at the bulges imposed by turbulent motions, correspond to strongly positive shear values and positive u^+ levels, presented in Fig. 9(*a*). According to the quadrant analysis of near-wall/interface turbulence structure [12], this scenario is the signature of sweep events through which the surface renews its structure, leading to high scalar transfer rates. By controlling surface renewal throughout the migration of high momentum fluid towards the interface, sweep motions create regions of high interfacial shear stress, leading in turn to high heat transfer rates. The scalar transfer rate reaches its peak value when the sweep impinges on the surface; during the decay time the diffusive layer saturates by the actions of molecular diffusion. On the other hand, increasing Pr produces a much finer thermal streaky structure and a decrease in heat transfer rate (note that the scale of the plots changes with Pr).

3.4 Temperature Variance. As the turbulent kinetic energy represents an integral measure of the energy associated with the fluctuating velocity field, the variance of the fluctuating temperature $\overline{\theta^2}$ may be regarded as the energy carried by the fluctuating temperature field. The equation for the evolution of the temperature variance can be written in compact form (see, for example, Nagano [25]) as

$$\frac{D\overline{\theta^2}}{Dt} = \mathcal{D}_\theta + \mathcal{T}_\theta + \mathcal{P}_\theta - \varepsilon_\theta \tag{20}$$

where D/Dt is the substantial derivative. The first and second terms on the right-hand side of this equation represent the diffusion by molecular actions and the diffusion due to turbulent transport, respectively. The third term is the production of $\overline{\theta^2}$ by the interactions between heat fluxes and mean temperature gradients. The last contribution represents the dissipation of the variance.

Figure 10 presents the budget terms obtained, for the gas side, from the present DNS. For the smaller Prandtl numbers, Pr=1 and 5, results are again compared to the data of Kawamura et al. [5]. For Pr=1, there are only small differences in the contributions to the balance (Fig. 10(*a*)), which conforms with previous results regarding the thickness of the thermal and momentum boundary layers and averaged heat fluxes. The effects of interfacial motion on the fluctuating thermal field are negligible at this Prandtl number. As the molecular Prandtl number increases (Fig. 10(*b*)), minor deviations from the wall-bounded flow data begin to appear, in particular concerning the production and turbulent diffusion terms. A comparison of the averaged normal heat fluxes in Fig. 7(*b*) explains why the production in wall flow is stronger than in the flow over the deformable interface.

The budget for Pr=10 presented in Fig. 10(*c*) indicates that the contribution of the production term becomes important with increasing Prandtl number, which is also true of the dissipation. In particular, these two contributions can be compared to the results of Na et al. [7] (their Figs. 7 and 13), which also show the values of $\mathcal{P}_\theta$ and ε_θ at the wall to increase drastically for Pr=10. The behavior of the dissipation in the diffusive thermal sublayer appears to be much more flat than for the case of the wall flow, and the starting value is also smaller.

3.5 Turbulent Heat Fluxes. In turbulence modeling, the most sophisticated approach accounting for the effects of turbulence-induced stresses in the heat transport consists in solving the transport equation for the turbulent heat fluxes, $\overline{u_i\theta}$, rather than resorting to the eddy diffusivity concept. In compact form, this transport equation can be written as

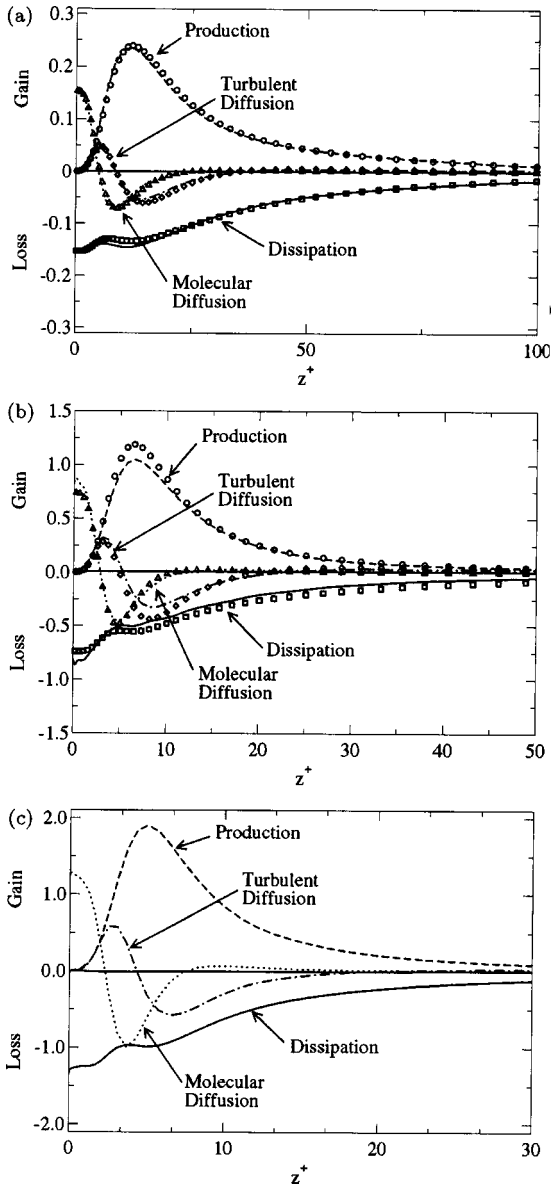

Fig. 10 Budget for the temperature variance in the near interface/wall region. Lines are used to identify the results of the present DNS and symbols to identify the wall-bounded DNS results of Kawamura et al. [5]. (*a*) Pr=1; (*b*) Pr=5; (*c*) Pr=10.

$$\frac{\mathrm{D}\overline{u_i\theta}}{Dt} = \mathcal{P}_i^\theta + \Pi_i^\theta + \mathcal{D}_i^\theta - \varepsilon_i^\theta \tag{21}$$

where the first term, $\mathcal{P}_i^\theta$, represents the mean flow production due to the combined actions of mean temperature gradients and mean velocity gradients. The second term is the pressure-temperature correlation, $\Pi_i^\theta \equiv -\overline{\theta \nabla p}$. The third contribution, $\mathcal{D}_i^\theta$, designates the diffusive transport comprising molecular, $\mathcal{D}_i^{m\theta}$, and turbulent counterparts, $\mathcal{D}_i^{t\theta}$. The last term, ε_i^θ, refers to the dissipation of turbulent heat flux (see, for example, Kasagi et al. [4] or Nagano [25] for the exact definition of each contribution).

Budgets of the streamwise heat flux, $\overline{u^+\theta^+}$, for the gas flow data obtained by the present DNS were compared (results not included here) to the channel-flow data of Kawamura et al. [5], for Pr=1 and 5. The comparison revealed the same behavior as observed before: the production becomes more important with increasing Pr, the molecular diffusion dominates as a positive con-

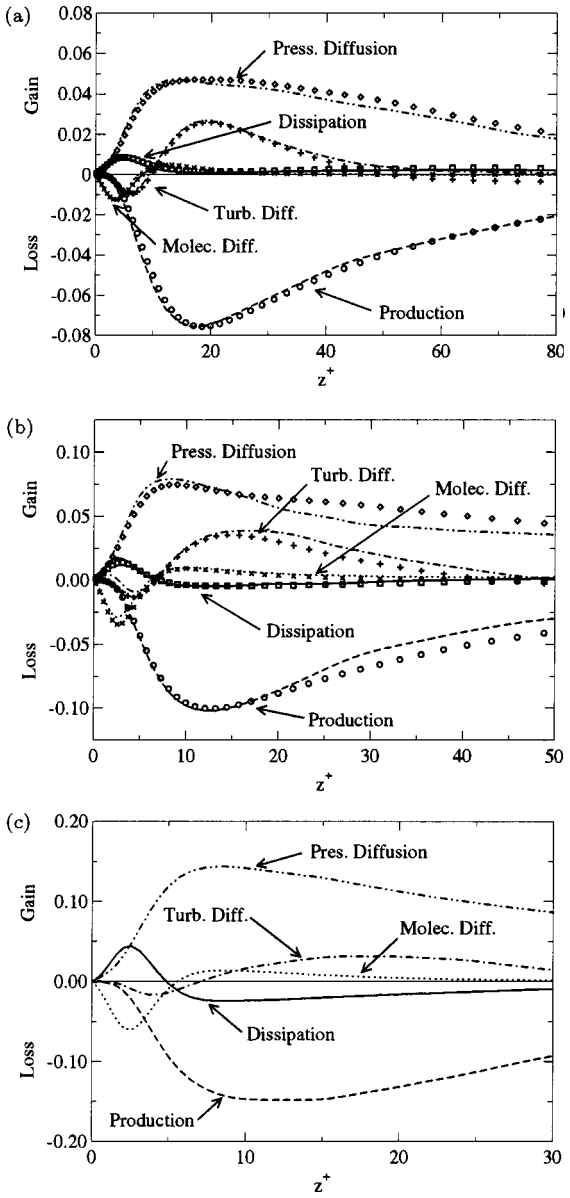

Fig. 11 Budget for the vertical turbulent heat flux in the near interface/wall region. Lines are used to identify the results of the present DNS and symbols to identify the wall-bounded DNS results of Kawamura et al. [5]. (*a*) Pr=1; (*b*) Pr=5; (*c*) Pr=10.

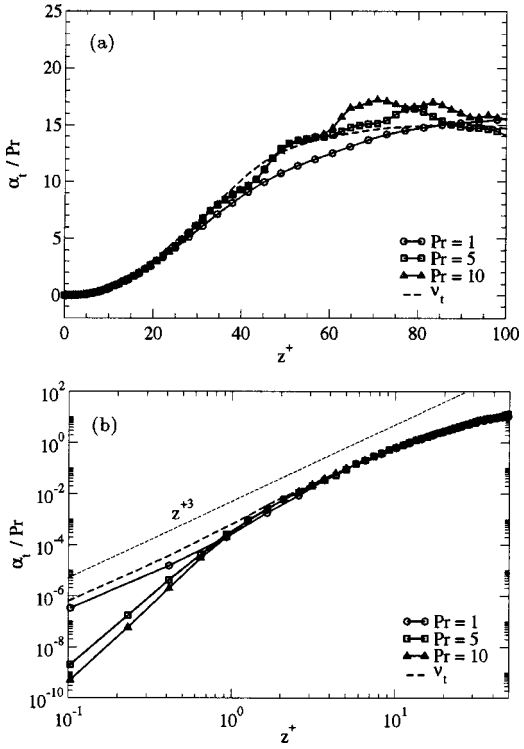

Fig. 12 (*a*) Turbulent diffusivity; and (*b*) Turbulent diffusivity in the vicinity of the deformable interface.

tribution in the diffusive sublayer and is balanced by the dissipation, while away from the wall/interface the production is balanced by the dissipation. The behavior of the dissipation, ε_i^θ, was particularly interesting: for Pr=1 its level gradually decreases away from the wall/interface, whereas for Pr=5 and 10 it marks a sharp drop at locations around the edge of the diffusive sublayer.

The effect of varying Prandtl number on the wall/interface-normal heat flux balance, $\overline{w^+\theta^+}$, is discussed in relation to Fig. 11, comparing the wall and the present deformable interface databases. Again, the production, which is negative in this case, gains in importance with increasing Pr, with the peak location always moving closer to the wall. In contrast to the streamwise component, the production in the normal direction is balanced by the pressure-gradient correlation $\Pi_3^\theta \equiv -\overline{\theta \partial_z p}$, and to a small extent by the turbulent diffusion $\mathcal{D}_3^{t\theta}$. The dissipation again shows an interesting behavior: the peak value of ε_3^θ in the diffusive sublayer increases with the Prandtl number. For Pr=1 the dissipation converges asymptotically almost to zero at $z^+ \approx 20$. For higher Prandtl numbers, the sign of ε_3^θ reverses exactly where the molecular and turbulent diffusion contributions change sign, too, indicating that in some flow regions the dissipation contributes positively as a gain. This was already revealed by Kasagi et al. [4] and Kawamura et al. [5], and was attributed to the fact that the dissipation takes place in the large-scale structures.

3.6 Turbulent Thermal Diffusivity. Turbulent thermal diffusivities were determined by averaging the thermal stress data and temperature gradients in the homogeneous directions and in time. The turbulent thermal diffusivity, α_t, was defined by applying the simplified Gradient Diffusion Hypothesis (GDH)

$$\overline{w^+\theta^+} = -\alpha_t \frac{d\Theta^+}{dz^+}. \tag{22}$$

The impact of varying Pr on the distribution of eddy diffusivity scaled by Pr is shown in Fig. 12(*a*), where the eddy viscosity—determined by use of GDH—is also included for comparison. For Pr=1 the data show the natural increase of α_t with distance to the interface, converging towards 15.5 at $z^+=100$. An increasing Prandtl number has no effect on α_t in the region close to the interface ($z^+<40$), but a larger one away from it. The eddy diffusivity is shown to gain almost 30% in this flow region. An attempt to infer values of the turbulent Prandtl number from this plot would not be conclusive, owing to the ragged profiles of α_t in the core flow region. Again, there is no clear picture on the exact dependence of α_t on Pr away from the interface.

The limiting behavior of the thermal diffusivity in the vicinity of the deformable interface is presented in Fig. 12(*b*), where the turbulent diffusivity for momentum is also included. For Pr=1 both α_t and ν_t vary with z^{+3}, as in wall flows. This again lends support to the hypothesis that the interface appears to the lighter phase like a wall. On the other hand, the result confirms the analogy between the diffusivities of momentum and heat for Pr=1.

However, at the same time it is noted that the slope of $\alpha_t/z^{+n}(n>3)$ increases with Pr as the interface is approached. This result suggests that $\alpha_t \sim z^{+3}$ cannot be justifiably generalized. The results of Na et al. [7] reveal the existence of a conductive layer at the wall, where α_t/z^{+3} appears to be constant, although it is decreasing with increasing Pr.

In summary, deformable, sheared interfaces populated by capillary waves with small wavelength play a similar role in heat transfer as solid walls. In particular, the near-interface limiting behavior is such that the normal velocity varies quadratically with the distance to the interface, and therefore the shear stress $\overline{u^+w^+}$ and the heat flux $\overline{w^+\theta^+}$ vary with z^{+3}. The scaling for α_t is, however, strongly tied to the Prandtl number, in that the variation with z^{+3} holds only for Pr=1. For Pr=5 and 10, on the other hand, the variation is proportional to z^{+n}, where $n>3$.

4 Concluding Remarks

Turbulent heat transfer across a mobile, sheared gas-liquid interface has been studied using direct numerical simulation. The purpose of the investigation was to examine the impact of the interfacial dynamics on turbulent heat transfer, and to investigate the influence of the Prandtl number on the transports by comparing the results to existing wall flow data. The motivation arose from the fact that investigations dealing with turbulent scalar transfer have focused on simple configurations involving rigid, flat surfaces, while in multicomponent systems the flow necessarily involves interfaces that are neither flat nor rigid.

The flow system studied comprises counter-flowing gas and liquid phases, each at a shear-based Reynolds number of 171. The interface deformations were limited to capillary-wave ripples with waveslope $ak=0.01$. Since, for high density ratios, interfaces play a role similar to that of a solid boundary, emphasis has been placed on the gas side. For both Pr=1 and Pr=5 the flux intensity near the deformable interface was found to be higher than at the wall. This implies that the interfacial dynamics leads to an increase in the vertical THF as compared to its value near the rigid wall. The explanation for this difference is that the waves enhance the velocity fluctuating field normal to the interface, as was revealed in [15]. The effect of Prandtl number (Pr=1, 5, and 10) on the averaged heat flux, the temperature variance, the eddy diffusivity, and the heat transfer scaling laws has been examined.

The changes in Pr were indeed found to affect the average results, but in very much the same way as in available wall flow data. This was particularly true for the way the thickness of the diffusive sublayer reduces with increasing Pr, and in reference to the induced influence on the production of heat flux and variance. It was also noticed that the pressure diffusion and dissipation contributions to the normal heat flux balance change with varying Prandtl number. The most relevant statistical quantities were found to scale with the friction velocity. This is an important result, since the capillary waves are expected to modify the local rate of heat transfer only through a reduction of the frictional drag in favor of form drag. This tendency accentuates with increasing waveslope caused by increasing u_*. In the present case, the imposed shear velocity at the beginning of the computations led to a ratio of frictional drag to total drag (including form drag) of 0.98. Another important result is the appreciable effect of Pr on $\overline{\theta^{+2}}$, and also on the thermal time scale $\tau_\theta \equiv \overline{\theta^{+2}}/\epsilon_0$ (results not included), indicating that the range of spectral functions for the thermal fluctuating field increases with Pr.

The scaling law for the normalized heat transfer velocity K^+ on the gas side suggests an approximate $\mathrm{Pr}^{-3/5}$ relationship, varying between $\mathrm{Pr}^{-1/2}$ for free surfaces and $\mathrm{Pr}^{-2/3}$ for immobile interfaces and much higher Prandtl numbers. The parameterization of the heat transfer rates based on the surface renewal theory delivers values for the constant of proportionality and the Pr-power that conform with both the Leveque and the Polhausens boundary layer solutions. A close inspection of the transfer rates reveals a strong and consistent relationship between the transfer rate, the frequency of sweeps impacting the interface, the interfacial velocity streaks, and the interfacial shear stress. Similarly to what is observed in wall flows, for Pr=1 the turbulent viscosity/diffusivity was found to asymptote with z^{+3}. For higher Pr, however, the scaling was seen to change to z^{+n}, with $n>3$. In the viscosity-affected layer the assumption that $\alpha_t \sim \nu_t$ was found to hold in this context, too, whereas in the outer core flow, α_t was greater than ν_t, and no clear picture emerged as to the distribution of the turbulent Prandtl number.

The present study has addressed only some of the many issues of this complex problem. It would be intriguing to see how statistical quantities scale with higher imposed shear velocities, i.e., in the presence of higher amplitude waves.

Acknowledgments

The computations were performed on the NEC SX-5 at the Swiss Center for Scientific Computing (CSCS) in Manno, Switzerland; in particular Marco Consoli is acknowledged for his help. Prof. A. Soldati, University of Udine, is gratefully acknowledged for his useful suggestions. The authors wish to thank Dr. V. De Angelis, University of California, Santa Barbara, who made available the original isothermal version of the DNS code employed in this study.

References

[1] Komori, S., Nagaosa, R., and Murakami, Y., 1993, "Turbulence Structure and Mass Transfer Across a Sheared Air-Water Interface in Wind-Driven Turbulence," J. Fluid Mech., **249**, p. 161.
[2] Rashidi, M., Hetsroni, G., and Banerjee, S., 1992, "Wave-Turbulence Interaction in Free-Surface Channel Flows," Phys. Fluids A, **4**, p. 2727.
[3] Danckwerts, P. V., 1951, "Significance of Liquid Film Coefficients in Gas Absorption," Ind. Eng. Chem., **43**, p. 1460.
[4] Kasagi, N., Tomita, Y., and Kuroda, A., 1992, "Direct Numerical Simulation of Passive Scalar Field in a Turbulent Channel Flow," ASME J. Heat Transfer, **114**, p. 598.
[5] Kawamura, H., Ohsake, K., Abe, H., and Yamamoto, K., 1998, "DNS of Turbulent Heat Transfer in Channel Flow With Low to Medium-High Prandtl Number," Int. J. Heat Fluid Flow, **19**, p. 482.
[6] Lyons, S. L., Hanratty, T. J., and McLaughlin, J. B., 1991, "Large-Scale Computer Simulation of Fully Developed Turbulent Channel Flow With Heat Transfer," Int. J. Numer. Methods Fluids, **13**, p. 999.
[7] Na, Y., Papavassiliou, D. V., and Hanratty, T. J., 1999, "Use of Direct Numerical Simulation to Study the Effect of Prandtl Number on Temperature Fields," Int. J. Heat Fluid Flow, **20**, p. 187.
[8] Campbell, J. A., and Hanratty, T. J., 1983, "Mechanisms of Turbulent Mass Transfer at Solid Boundaries," AIChE J., **29**, p. 221.
[9] McCready, M. J., Vassiliadou, E., and Hanratty, T. J., 1986, "Computer Simulation of Turbulent Mass Transfer at a Mobile Interface," AIChE J., **32**, p. 1108.
[10] Calmet, I., and Magnaudet, J., 1997, "Large-Eddy Simulation of High-Schmidt Number Mass Transfer in a Turbulent Channel Flow," Phys. Fluids, **9**, p. 438.
[11] Piller, M., Nobile, E., and Hanratty, T. J., 2002, "DNS Study of Turbulent Transport at Low Prandtl Numbers in a Channel Flow," J. Fluid Mech., **458**, p. 419.
[12] Lombardi, P., De Angelis, V., and Banerjee, S., 1996, "Direct Numerical Simulation of Near-Interface Turbulence in Coupled Gas-Liquid Flow," Phys. Fluids, **8**, p. 1643.
[13] De Angelis, V., Lombardi, P., and Banerjee, S., 1997, "Direct Numerical Simulation of Turbulent Flow Over a Wavy Wall," Phys. Fluids, **9**, p. 2429.
[14] De Angelis, V., Lombardi, P., Andreussi, P., and Banerjee, S., 1997, "Micro-Physiscs of Scalar Transfer at Air-Water Interfaces," in *Proceedings of Wind-Over-Wave Couplings: Perspectives and Prospects*, S. G. Sajjadi, N. H. Thomas, and J. C. R. Hunt, eds., Oxford University Press.
[15] Fulgosi, M., Lakehal, D., Banerjee, S., and De Angelis, V., 2003, "Direct Numerical Simulation of Turbulence in a Sheared Air-Water Flow With Deformable Interface," J. Fluid Mech., **482**, p. 319.
[16] Delhaye, J. M., 1974, "Jump Conditions and Entropy Sources in Two-Phase Systems. Local Instant Formulation," Int. J. Multiphase Flow, **1**, p. 305.
[17] Lakehal, D., Meier, M., and Fulgosi, M., 2002, "Interface Tracking Towards the Direct Simulation of Heat and Mass Transfer in Multiphase Flows," Int. J. Heat Fluid Flow, **23**, p. 242.
[18] Temam, R., 1979, *Navier-Stokes Equations*, North-Holland, Amsterdam.
[19] Tiselj, I., Bergant, R., Mavko, B., Bajsic, I., and Hetsroni, G., 2001, "DNS of Turbulent Heat Transfer in Channel Flow With Heat Conduction in the Solid Wall," ASME J. Heat Transfer, **123**, p. 849.

[20] Phillips, O. M., 1997, *The Dynamics of the Upper Ocean*, Cambridge University Press, Cambridge, UK.
[21] Tiselj, I., Pogrebnyak, E., Li, C., Mosyak, A., and Hetsroni, G., 2001, ''Effect of Wall Boundary Condition on Scalar Transfer in a Fully Developed Turbulent Flume,'' Phys. Fluids, **13**(4), p. 1028.
[22] Papavassiliou, D. V., and Hanratty, T. J., 1997, ''Transport of a Passive Scalar in a Turbulent Channel Flow,'' Int. J. Heat Mass Transfer, **40**, p. 1303.
[23] Banerjee, S., 1971, ''A Note on Turbulent Mass Transfer at High Schmidt Numbers,'' Chem. Eng. Sci., **26**, p. 989.
[24] Lam, K., and Banerjee, S., 1992, ''On the Condition of Streaks Formation in a Bounded Turbulent Flow,'' Phys. Fluids A, **4**, p. 306.
[25] Nagano, Y., 2002, ''Modelling Heat Transfer in Near-Wall Flows,'' in *Closure Strategies for Turbulent and Transitional Flows*, B. Launder and N. Sandham, eds., Cambridge University Press.